NANO LETTERS

Letter

pubs.acs.org/NanoLett

Gate-Dependent Carrier Diffusion Length in Lead Selenide Quantum Dot Field-Effect Transistors

Tyler Otto,[†] Chris Miller,[†] Jason Tolentino,[‡] Yao Liu,[§] Matt Law,[‡,§] and Dong Yu*,[†]

[†]Department of Physics, University of California, Davis, California 95616, United States

[‡]Department of Chemical Engineering and Materials Science, University of California, Irvine, California 92697, United States

[§]Department of Chemistry, University of California, Irvine, California 92697, United States

Supporting Information

ABSTRACT: We report a scanning photocurrent microscopy (SPCM) study of colloidal lead selenide (PbSe) quantum dot (QD) thin film field-effect transistors (FETs). PbSe QDs are chemically treated with sodium sulfide (Na_2S) and coated with amorphous alumina (a-Al_2O_3) by atomic layer deposition (ALD) to obtain high mobility, air-stable FETs with a strongly gate-dependent conductivity. SPCM reveals a long photocurrent decay length of 1.7 μm at moderately positive gate bias that decreases to below 0.5 μm at large positive gate voltage and all negative gate voltages. After excluding other possible mechanisms including thermoelectric effects, a thick depletion width, and fringing electric fields, we conclude from photocurrent lifetime measurements that the diffusion of a small fraction of long-lived carriers accounts for the long photocurrent decay length. The long minority carrier lifetime is attributed to charge traps for majority carriers.

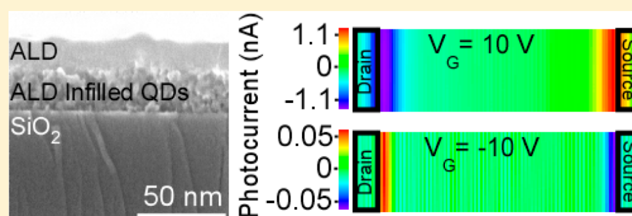

KEYWORDS: *Colloidal quantum dots, mobility, field-effect transistors, scanning photocurrent microscopy, carrier diffusion length*

Colloidal semiconductor quantum dots (QDs) have been intensively investigated for their potential use in novel electronic devices. Of particular interest is their use in third-generation photovoltaic devices and sensitive photodetectors.[1−3] The potential for low fabrication cost using scalable manufacturing processes such as ink jet printing make them attractive candidates for next-generation solar panels. Strongly confined QDs such as lead selenide (PbSe) also have the potential to benefit from tunable absorption spectra, multiple exciton generation (MEG), and/or hot carrier extraction.[4−7] Slow charge transport in QD arrays has been a bottleneck for realizing their efficient optoelectronic applications. It has been demonstrated that surface ligand exchange can significantly improve conductivity of colloidal QD thin films.[8−16] Air-stable and high-mobility QD thin films have also been achieved by infilling and overcoating QD films with atomic layer deposition (ALD).[17] Although promising steps have been made, major improvements are still necessary for QD solar cells to compete with commercial technologies. In particular, the carrier mobility and recombination lifetime in QD thin films must be substantially increased to maximize photocurrent collection.

Scanning photocurrent microscopy (SPCM) allows one to spatially resolve the optoelectronic properties of semiconductor nanowires and thin films[18−25] and can provide valuable information for understanding charge transport and recombination in QD solids. In SPCM, carriers locally injected by a tightly focused laser beam diffuse and/or drift toward electrical contacts and contribute to photocurrent if collected before charge recombination occurs. SPCM has been used to map the local electric field distribution and extract minority carrier diffusion lengths for a variety of semiconductor nanowires.[20,23] Recently, SPCM has been applied to image Schottky barriers in colloidal PbS QD thin films.[24] As locally injected electrons and holes can be driven by temperature gradients, electric fields, and carrier concentration gradients, it is often challenging to convincingly deconvolute the individual effects, leading to difficulty in interpreting SPCM data. Thus it is often necessary to utilize measurements of surface potential and photocarrier decay time with numerical modeling to correctly interpret the SPCM results and identify the dominant driving mechanism(s).

Here we report the optoelectronic characterization of air-stable PbSe QD field-effect transistors (FETs) that are chemically treated by sodium sulfide (Na_2S) and infilled with amorphous alumina (a-Al_2O_3).[17] The thin films exhibit ambipolar conduction with an electron field-effect mobility of ~5 $cm^2/(V\ s)$ and a hole mobility of ~0.1 $cm^2/(V\ s)$. Our devices show strong gate dependence in both conductivity and photocurrent profiles, allowing us to explore how carrier concentration and band bending at the contacts influence carrier transport and recombination. SPCM measurements reveal a gate voltage dependent photocurrent decay length as long as 1.7 μm under conditions of electron accumulation in the FET channel (positive gate bias). As a complementary

Received: January 8, 2013
Revised: June 17, 2013

 © XXXX American Chemical Society

technique, we have performed Kelvin probe microscopy (KPM) to characterize the surface potential profiles of the devices.[26,27] We have combined these measurements with time-resolved photocurrent measurements that indicate the presence of a long component to the carrier lifetime, as seen in previous studies of other types of QD films.[1,2] We supplemented these measurements with numerical temperature and electric field simulations. We attribute the long photocurrent decay length in these QD FETs to the diffusion of a small fraction of the minority carriers with a long charge recombination lifetime.

A mechanical dip coater mounted inside of a nitrogen filled glovebox (DC Multi-4, Nima Technology) was used to prepare PbSe QD films via a layer-by-layer procedure described in detail elsewhere.[17] The FETs were composed of lithographically defined electrodes (10 nm Cr/30 nm Au) on top of degenerately doped silicon covered with 300 nm of thermal oxide. The electrodes were 100 μm wide with a separation of 10 μm. The substrates were cleaned by sonicating in acetone and isopropanol and then dried under N_2 flow. The substrates were then alternately dipped into a 2 mg mL^{-1} solution of QDs in dry hexane and then a 0.5 mM solution of Na_2S in dry methanol. A third beaker containing neat dry methanol was used to rinse the films after each dip in the sulfide solution to remove any residual Na_2S. Finally, amorphous Al_2O_3 (a-alumina) was deposited by ALD onto the QD thin films using alternating pulses of trimethylaluminum and water with a substrate temperature of 54 °C and an operating pressure of 90 mTorr. Pulse and purge times were 20 ms and 90−120 s, respectively. The thickness was confirmed by profilometry and scanning electron microscopy (Figure 1a). The ALD infilling leads to films that are indefinitely stable in air even with exposure to laser illumination. In this study, we used 30−40 nm thick films of 6.3 nm diameter QDs with a first exciton peak of 0.67 eV in solution.

In our SPCM setup, a tightly focused laser is raster-scanned across the surface of the QD FET, while the photocurrent and the specular reflectance are simultaneously recorded as a function of illumination position to construct a photocurrent map (Figure 2a). A coherent 532 nm CW laser is focused onto

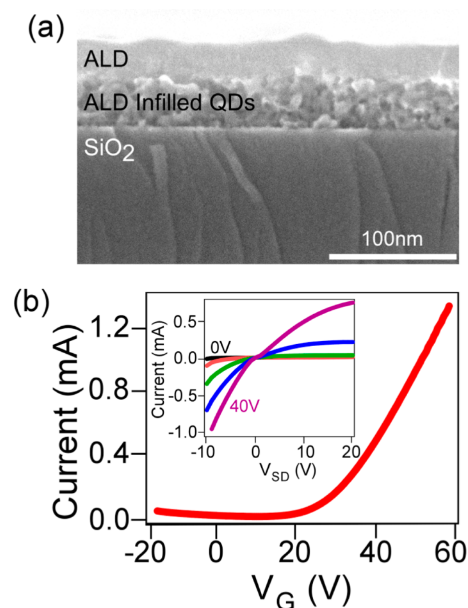

Figure 1. (a) Cross-sectional SEM image of a PbSe QD thin film infilled with alumina using ALD. (b) Current at V_{SD} = +10 V as a function of gate voltage for device **D1**. Inset: I−V curves for V_G = 0−40 V in 10 V steps.

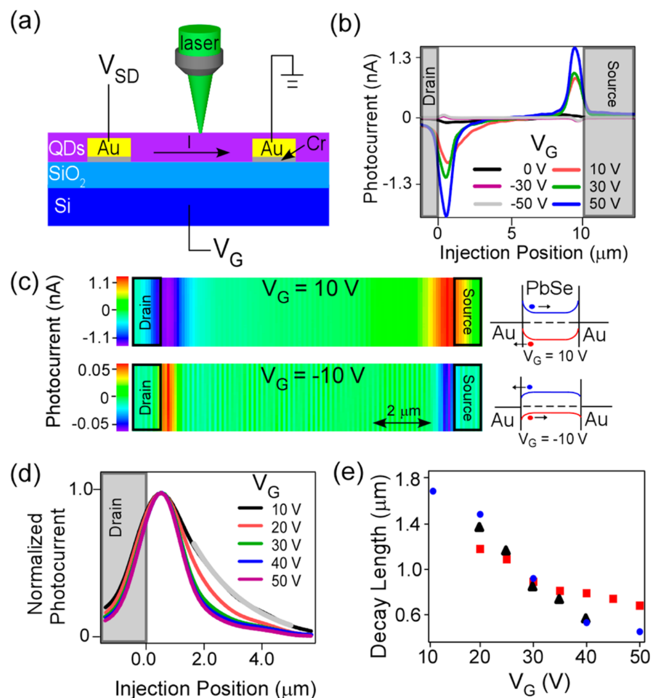

Figure 2. SPCM investigation of a representative ALD-infilled PbSe QD FET (**D1**). (a) Cartoon of the SPCM setup. The direction of positive current is to the right. (b) Photocurrent line scans at V_{SD} = 0 V and various values of V_G. (c) Zero-bias SPCM images and associated band diagrams for a device at V_G = +10 V and −10 V. (d) Normalized zero-bias photocurrent line scans acquired near the drain contact. The gray curve is an exponential fit of the V_G = 10 V data. The shaded area denotes the location of the contact. (e) Photocurrent decay length extracted for three different devices as a function of gate voltage. Note that the photocurrent at V_G = 10 V in the other two devices is too small to extract l and thus their data begin from V_G = 20 V.

the FET channel by a NA0.95 100× objective lens in a BX51 Olympus microscope. The full width at half-maximum (fwhm) of the Gaussian beam is measured to be $d_{laser} \approx 0.5$ μm from the photocurrent cross section perpendicular to a nanowire, as described elsewhere.[20] The laser power is 20 μW, resulting in a peak intensity of 7 kW/cm^2. The electrical measurements are performed using a DL 1211 preamplifier and a National Instruments data acquisition system (DAQ) controlled by a Labview program. An optical chopper (Thorlabs) and a lock-in amplifier (EG&G model 5209) are used to obtain SPCM images. The time-resolved photocurrent measurements are carried out by using the optical chopper, a Tektronix digital oscilloscope, and an NF Electronic Instruments BX-31A preamplifier. The optical chopper chops the laser beam at ∼1 kHz. The temporal resolution is about 10 μs limited by the chopping speed. The photoinduced current is amplified by the preamplifier and recorded by the oscilloscope to obtain the time decay. KPM is performed by a VEECO Dimension 3100 atomic force microscope (AFM) with a conductive cantilever.

QD FETs fabricated by Na_2S ligand exchange and ALD infilling show a conductivity of $\sigma \approx 1$ S/cm at zero gate voltage (V_G = 0 V) and low source-drain voltage (V_{SD} = 1 V). The QD thin film is deposited on top of the Cr/Au electrodes as shown

dx.doi.org/10.1021/nl401698z | Nano Lett. XXXX, XXX, XXX−XXX

in Figure 2a. The current−voltage ($I-V$) curves of a typical device (herein labeled **D1**) are nearly linear at low V_{SD} (Figure 1b inset), which indicates nearly ohmic contacts. Minimal band bending is expected for the Au/PbSe QD contacts because of the high work function of Au. Gate voltage scans show that these devices are ambipolar (Figure 1b). We extract the field-effect mobility of the carriers from the gate-dependent conductance. The electron and hole mobility differs by more than 1 order of magnitude, with $\mu_e \approx 5$ cm^2/(V s) and $\mu_h \approx 0.1$ cm^2/(V s), which are extracted from the linear part of the gate sweep (Figure 1b). The electron concentration is estimated to be 2×10^{18} cm^{-3} at $V_G = 50$ V assuming that carriers are uniformly distributed in the 30 nm thick film. This value increases to $\sim 10^{19}$ cm^{-3} if we assume the accumulation layer is confined to one QD monolayer (~7 nm thick) at the SiO_2 interface. Because the conductance drops by 2 orders of magnitude from $V_G = 50$ V to $V_G = 10$ V, we can estimate that the carrier concentration is $2 \times 10^{16} - 10^{17}$ cm^{-3} at $V_G = 10$ V.

SPCM results for the same device (**D1**) are shown in Figure 2. When $|V_G| < 10$ V, the zero-bias photocurrent (i.e., at $V_{SD} = 0$) is very low (<10 pA) under a laser intensity of 7 kW/cm^2 (Figure 2b). When $V_G \geq 10$ V, negative (positive) photocurrent is clearly observed when the laser is scanned close to the drain (source) contact (Figure 2b). The magnitude of the photocurrent increases at more positive V_G. Both the photocurrent magnitude and decay length are much smaller at negative V_G (Figure 2b,c). The photocurrent is negligible on top of the metal electrodes for all V_G, which is likely due to screening of the electric field by the electrodes and/or fast charge recombination at the metal surface.[28] We also note that V_g scans can lead to hysteresis in both the dark conductivity and photocurrent profiles. This can be understood by considering charge accumulation in trap states on the surfaces of the QDs. The focus of this study is steady state behavior. By allowing the films to "rest" for several minutes prior to performing SPCM scans, differences between repeated V_g scans at the same gate voltage became negligible.

The photocurrent near the metal contacts of a device is often driven by band bending at the contacts.[18] The very low photocurrent at $V_G = 0$ V indicates that both the conduction and valence bands are nearly flat and therefore the internal electric field at the contacts is too weak to efficiently separate injected charge carriers. The application of positive (negative) V_G introduces negative (positive) charge carriers and pushes down (up) the bands, causing upward (downward) band bending in the semiconductor toward the metal contacts (see band diagrams in Figure 2c). When $V_G \geq 10$ V, a sufficiently large band bending is induced by the gate voltage such that photocurrent is clearly observable (Figure 2b). At higher V_G, the band bending increases and leads to more efficient charge separation and thus a larger photocurrent, as shown in Figure 2b. The shift in the Fermi level, and in-turn the degree of band bending at the contacts, can be estimated as $\Delta E_F = k_BT \ln(G_{50V}/G_{0V}) \approx 0.14$ eV, where k_B is the Boltzmann constant, T is the temperature, and G_{50V} (G_{0V}) is the conductance at $V_G = 50$ V (0 V). This expression can be derived from $\sigma = qn\mu_e$ and $n = n_0 \exp[(E_F - E_i)/(k_BT)]$, where σ is the conductivity, n is the electron density, n_0 is the intrinsic electron density, E_F is the Fermi level, and E_i is the Fermi level in an intrinsic semiconductor. We have assumed that the mobility is constant with gate voltage.

From the photon flux of the laser and the magnitude of the photocurrent, we estimate a charge collection efficiency of $\eta_{cc} \sim 0.05\%$ at $V_G = 50$ V (using a current of 1.6 nA, excitation power of 20 μW, and absorption length of 72 nm for 532 nm light). We note that η_{cc} shows some variability from device to device. In a different device (**D2**) shown in Figure 3a, we have measured a 40 nA photocurrent at $V_{SD} = 0$ V and $V_G = 40$ V, giving a much higher η_{cc} of ~1%. The low η_{cc} indicates that only a small fraction of the injected carriers are collected and the majority of injected carriers recombine before reaching the contacts. The Au electrodes used in this study are expected to make ohmic contact to PbSe QD thin films. Although the application of V_G can induce band bending at such contacts, the electric field is still weaker than that in the junction between PbSe QDs and low work function metals such as Al often used in solar cells. Another obstacle for charge collection is the energy barrier induced by V_G at the opposite contact (see band diagram in Figure 2c), resulting in back-to-back barriers that further lowers the photocurrent.[23]

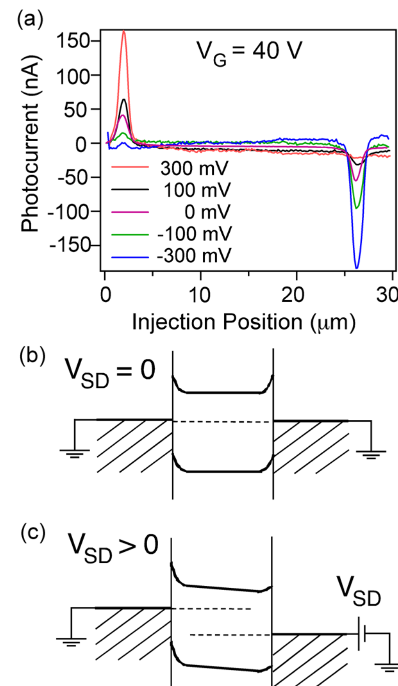

Figure 3. Photocurrent line scans at different V_{SD} for device **D2**. (a) Photocurrent line scan at $V_G = 40$ V and $V_{SD} = -300$ mV to +300 mV. The dark current has been subtracted from all photocurrent traces. (b, c) Band diagrams at $V_{SD} = 0$ V and $V_{SD} > 0$ V.

The photocurrent decay profile fits well to a simple exponential, $I = I_0 \exp(-x/l)$, with a decay length $l = 1.7$ μm at $V_G = 10$ V (device **D1**, Figure 2d). The photocurrent deviates from the exponential fit near the peak maximum because part of the laser spot excites the QDs on top of the Au electrode and does not contribute to photocurrent. Increasing V_G further leads to a reduction in l (Figure 2d, e). The photocurrent decay length decreases from 1.7 μm at $V_G = 10$ V to 0.5 μm at $V_G = 50$ V, which is close to the spatial resolution of our SPCM (Figure 2c,d). Importantly, a measurable decay length is observed only at positive V_G, while the decay length is always shorter than the spatial resolution of our SPCM at negative V_G. The photocurrent at negative V_G is more than 1 order of magnitude smaller. This trend of gate-dependent photocurrent decay length has been observed in all eight

dx.doi.org/10.1021/nl401698z | Nano Lett. XXXX, XXX, XXX−XXX

devices we have studied. Figure 2e shows l as a function of V_G for three representative devices.

To further confirm that the bands bend at the contacts under applied V_G, we have measured SPCM profiles at different values of V_{SD} for device **D2**. When $V_G < 20$ V, the photocurrent at the contacts is too small compared with the dark current to determine how the photocurrent changes with V_{SD}. However, at $V_G > 20$ V, we can clearly see that photocurrent strongly depends on V_{SD} (data at $V_G = 40$ V shown in Figure 3a). When V_{SD} is applied, the photocurrent on the high potential (low potential) contact is suppressed (enhanced). This is because the external field generated by V_{SD} is in the opposite (same) direction of the internal electric field at the high-potential (low-potential) contact and thus suppresses (enhances) the band bending (see band diagrams in Figure 3b,c). The contact band bending under V_G is characteristic of Schottky type contacts. Previous simulations indicate that the photocurrent in devices with at least one Schottky contact is dominated by minority carrier diffusion current.[23] Hence, we can extract the minority carrier diffusion length from the measured photocurrent line scans if carrier diffusion is indeed the dominant transport mechanism.

In general, the photocurrent can be driven by electric fields, temperature gradients, and charge concentration gradients. Thus, to determine the origin of this long photocurrent decay length, we consider all three possible mechanisms. We first rule out the possibility that the first two mechanisms account for the long decay length. Then we substantiate charge diffusion as the most likely mechanism.

1. Internal Electric Fields. A long SPCM decay length was recently reported in a study of PbS QD thin films and attributed to a ∼1.8 μm wide depletion layer near a Ti contact.[24] This surprisingly thick depletion layer was attributed to a reduced free carrier concentration due to the device geometry and surface states at the SiO_2 interface. However, in our case, we believe the photocurrent decay length is unlikely to be caused by the depletion width at the contacts. We can estimate the carrier concentration from our gate dependence to be 2×10^{16}−10^{17} cm^{-3} at $V_G = 10$ V. We have estimated the band bending magnitude to be ∼0.14 eV at $V_G = 50$ V. The potential barrier should be much smaller at $V_G = 10$ V. Even if we use a conservative upper limit of 100 mV and take an effective QD thin film dielectric constant of 30,[29] the depletion width is expected to be only 60−130 nm, much shorter than the observed decay length of 1.7 μm.

It is also possible that a fringing electric field is induced at the contacts by the applied gate voltage. At the edges of the source/drain electrodes on top of the SiO_2, the gate-induced electric field can have a horizontal component that is capable of inducing photocurrent in the film. To quantitatively model this behavior, we used a 2D finite element differential equation solver (Agros2D). The device geometry and estimated electrical properties were mimicked. We used a dielectric constant of $\varepsilon = 30$ for the QD thin film, grounded the drain/source electrodes, and applied a potential to the back gate. For simplicity, we treated the QD thin film as an insulator. We found that the electric field component (E_x) parallel to the film has a decay length of ∼0.3 μm, much shorter than the observed l (Figure 4a). A conductive QD thin film will likely screen this field, reduce the decay length, and lead to an even narrower field distribution.

To experimentally determine the depletion width and the presence of any sources of electric field near the contacts, we measured the surface potential of several devices with KPM. At $V_{SD} = V_G = 0$ V, the surface potential is flat to within 10 mV over the entire film, including the film on top of the electrodes. When $V_G = +5$ V is applied, KPM shows a surface potential difference of ∼0.1 V near the contacts with a spatial extension about 0.5 μm into the QD film (Figure 5). Note that this value is likely to be an upper limit of the actual internal electric field distribution, as the KPM resolution is limited by the finite tip size and the long-range of the electrostatic force. At $V_G = -5$ V, the surface potential switches sign near the contacts. This extension of the internal electric field is too short to account for the long photocurrent decay length. Higher gate voltages

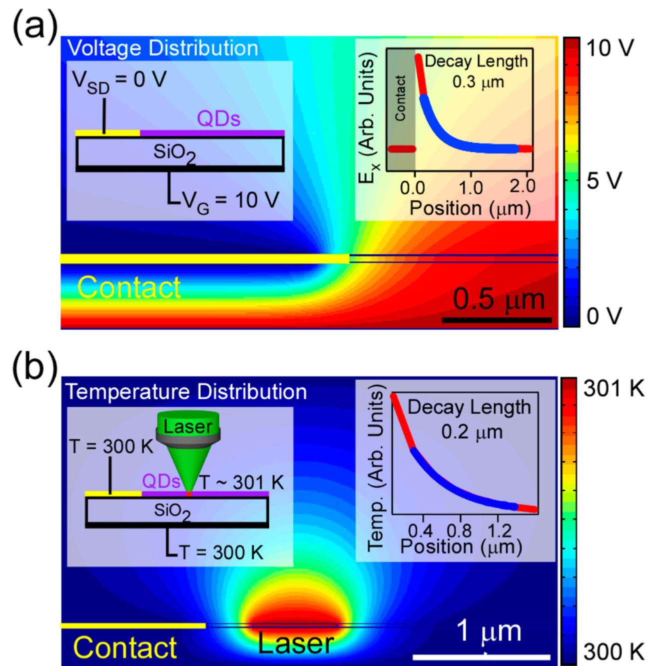

Figure 4. (a) Simulated electric field distribution in a three-terminal QD FET at $V_{SD} = 0$ V and $V_G = +10$ V. Left inset: cartoon of the QD FET. Right inset: simulated horizontal component of electric field (E_x) in the QD thin film. The blue curve is an exponential fit. (b) Simulated temperature distribution in a QD FET with the laser positioned 1 μm from the contact. Left inset: cartoon of the QD FET under a focused laser beam. Right inset: simulated temperature at the edge of the contact as a function of laser position in the channel.

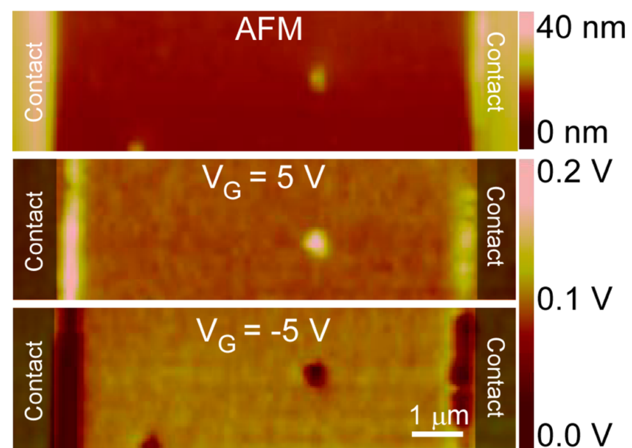

Figure 5. AFM and KPM images of a QD FET at $V_{SD} = 0$ V.

resulted in distorted AFM and KPM images, presumably due to the strong interactions between tip and surface induced by the large gate field.

2. Thermoelectric Effects. PbSe QD films can have a Seebeck coefficient higher than that of bulk PbSe. For 6 nm QDs, the Seebeck coefficient has been reported to be nearly 1 mV/K.[30] As an order-of-magnitude estimate, if the QD/Au junction is heated by 1 K due to laser illumination, a potential difference of 1 mV will be induced, resulting in a 100 pA photothermal current for a film resistance of 10 MΩ, which is close to the measured photocurrent value. The thermoelectric current is also expected to reverse direction with gate polarity as the film switches from n-type to p-type. The magnitude of the thermoelectric current is also expected to depend on V_G. As V_G increases, the film conductivity can be increased more than the decrease in Seebeck coefficient, leading to a net increase in thermoelectric current, in agreement with our observations.[31] When the laser spot is moved away from the junction, the junction temperature will decrease, leading to a reduction in the photocurrent. The determination of the decay length requires numerical modeling.

To extract the shape of the thermoelectric current profile, we simulate the temperature distribution within the QD thin film by solving the 2D thermal transport equation as a function of laser injection position using Agros2D (Figure 4b). As in the electrical field calculation, the device geometry and estimated thermal properties were mimicked. We used a thermal conductivity of 2.5 W/m·K for the QD film[31] and fixed the far end of the gold electrodes and the bottom of the SiO_2 layer to room temperature (300 K). We simulated the injection of a local heat flux corresponding to the absorbed power of our laser which caused the film temperature to increase by ~1 K over the width of the laser spot (~0.5 μm). Using the temperature difference between the two electrodes, we found that the magnitude of the thermally induced current is comparable with the observed peak photocurrent but the decay length is <0.2 μm, much shorter than the observed photocurrent decay length. This short decay length is caused by the low thermal conductivity of the QD film. The temperature at the QD-metal contact, which determines the thermoelectric current, decreases quickly when the heat source moves away from the contact in a thermally insulating film. In addition, because the thermal conductivity of PbSe is already quite low, the gate has minimal effect on the decay length. Even an order of magnitude change in thermal conductivity leads to a negligible change in decay length in the simulation.

The V_{SD} dependence provides additional evidence that the observed photocurrent does not originate from thermoelectric effects (Figure 3). The thermoelectric current is expected to depend on the temperature difference between the two contacts (and thus the laser heating power), but not on the potential difference between the two contacts.

3. Charge Diffusion. The observed photocurrent decay length is much longer than the estimated depletion width. Therefore, carrier drift under the Schottky electric field alone cannot account for the long decay length. Carrier diffusion must be involved to explain the observations. The charge carriers photogenerated outside the depletion region can diffuse into the depletion region and contribute to current. While the measured photocurrent decay length reflects a combination of thermoelectric effects, depletion width, and carrier diffusion length, it is dominated by the carrier diffusion length since other decay lengths are estimated to be significantly shorter. In fact, SPCM has been used to determine the minority carrier diffusion length in several types of nanowires.[20,23]

If the depletion width is small, the photocurrent decays as $I = I_0 \exp(-x/L_p)$ for an n-type film, where x is the distance from the contact and L_p is the minority carrier diffusion length. $L_p = (D_p\tau_p)^{1/2}$, where $D_p = \mu_p k_B T/q$ is the hole diffusion coefficient and τ_p is the hole lifetime. Using $\mu_p = 0.1$ cm^2/(V s) and $L_p = 1.7$ μm, we find that $\tau_p = 10$ μs. Thus, the observed 1.7 μm photocurrent decay lengths would require a surprisingly long lifetime of ~10 μs to allow the carriers to diffuse to the contact.

To obtain the lifetime, we measured the photocurrent decay at $V_{SD} = 0$ V. To do this, we rapidly blocked the laser beam focused near one contact with an optical chopper while monitoring the photocurrent on an oscilloscope. The photocurrent decay can be fit well by a single exponential (Figure 6a).

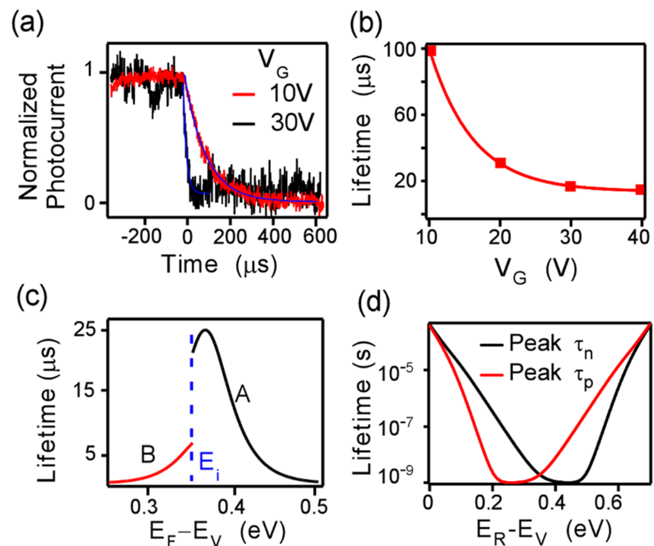

Figure 6. (a) Photocurrent time traces for device **D2** at $V_{SD} = 0$ V and different V_G after the excitation stops at $t = 0$ s. The blue curves are exponential fit to the data. (b) Photocurrent lifetime extracted from (a) as a function of V_G. (c) Simulated minority carrier lifetime as a function of the Fermi level relative to the valence band. E_i is the intrinsic Fermi level. The black curve is for the hole lifetime in an n-type film when $E_F > E_i$. The red curve is for the electron lifetime in a p-type film when $E_F < E_i$. A represents the Fermi level in the n-type regime, and B is in the p-type regime. (d) Maximum electron and hole lifetimes as a function of trap position. The data from these plots use the parameters listed in Table 1.

The extracted lifetime is 100 μs at $V_G = 10$ V and 16 μs at $V_G = 40$ V (Figure 6b). However, the 16 μs lifetime is limited by the speed of our optical chopper. The photocurrent is too small at $V_G < 0$ V to give definite measurements of lifetime in device **D2**. In another device (**D3**), the measured lifetime is 27 μs at $V_G = 40$ V, while the lifetime at $V_G = -40$ V is <12 μs (Figure S1).

Recombination lifetimes with components ranging from 10 μs to 70 ms have been previously observed in the photocurrent decay of colloidal QD films.[1,2] Our measured lifetimes confirm slow components of the photocurrent decay in our films. The shorter lifetime at higher V_G is consistent with the shorter photocurrent decay length measured by SPCM (Figure 2). On the other hand, the 100 μs lifetime is much longer than the 10 μs inferred from the SPCM data. This discrepancy is probably caused by the multiple lifetimes in the photocurrent decay. The relatively low temporal resolution of our setup prevents us from

dx.doi.org/10.1021/nl401698z | Nano Lett. XXXX, XXX, XXX−XXX

measuring the faster component of the photocurrent decay, which may dominate the SPCM signal.

While a majority of injected carriers rapidly recombine through midgap trap-assisted processes (and to a lesser extent Auger and radiative recombination), a small fraction recombine much more slowly via shallower trap sites, resulting in the observed photocurrent. Here we summarize two major observations from our SPCM and photocurrent decay measurements that support this conclusion: (i) minority carrier lifetime decreases with increasing V_G in n-type QD thin films (Figures 2d and 6a,b), and (ii) minority carrier lifetime is much shorter in p-type films than that in n-type films (Figure 2c and Figure S1). The Shockley–Read–Hall (SRH) model of nonradiative carrier recombination in the presence of trap sites provides a quantitative explanation for these two observations.[32] For simplicity, we consider trap sites with a single energy level. We also use the Boltzmann approximation for nondegenerate semiconductors. Under the assumption of low injection and a large number of single level trap sites, the electron lifetime (τ_n) and hole lifetime (τ_p) can be expressed as:[32]

$$\tau_p = \frac{\tau_{n0}(p_0 + p') + \tau_{p0}[n_0 + n' + N_R(1 + n_0/n')^{-1}]}{n_0 + p_0 + N_R(1 + n_0/n')^{-1}(1 + n'/n_0)^{-1}} \quad (1)$$

$$\tau_n = \frac{\tau_{p0}(n_0 + n') + \tau_{n0}[p_0 + p' + N_R(1 + p_0/p')^{-1}]}{n_0 + p_0 + N_R(1 + p_0/p')^{-1}(1 + p'/p_0)^{-1}} \quad (2)$$

where $\tau_{n0} = 1/(\nu S_n N_R)$ and $\tau_{p0} = 1/(\nu S_p N_R)$ are the electron and hole lifetimes when the trap sites are fully occupied, $n_0 = N_C \exp[(E_F - E_C)/k_BT]$ and $p_0 = N_V \exp[(E_V - E_F)/k_BT]$ are the free electron and hole densities, and $n' = N_C \exp[(E_R - E_C)/k_BT]$ and $p' = N_V \exp[(E_V - E_R)/k_BT]$ are the densities of free electrons and holes when $E_F = E_R$, respectively. For simplicity, we set $S_n = S_p$, where S_n (S_p) is the electron (hole) trap cross-section. The meanings and values of the physical parameters used in the calculation are listed in Table 1. The calculated lifetime as a function of E_F (Figure 6c) is in good agreement with both of our main experimental observations and similar to lifetimes observed in other semiconductors, such as doped Si and Ge crystals.[33,34] N_C, N_V, and ν are calculated using the effective mass of electrons in PbSe ($0.2m_e$). Other parameters are determined by comparing simulation results with the observed lifetimes. The lifetime is very sensitive to the energy of the trap sites. Trap states ~80 meV below the conduction band edge give reasonable agreement with our observations. Peak electron and hole lifetimes can vary by over 5 orders of magnitude as E_R shifts across the bandgap (Figure 6d). Shallower trap sites lead to slower recombination. In this simple model, we have assumed a single trap level. In reality, it is likely that many trap levels exists, which explains the observations of multiple components to the lifetime.[1,2] The presence of such shallow trap levels may be caused by an Urbach tail of states generated by the disordered QD films. These states are predicted to influence carrier dynamics.[35,36]

Table 1. Physical Parameters Used for Calculating Lifetime

symbol	physical meaning	value
E_G	bandgap	0.7 eV
N_C/N_V	effective density of states at the conduction/valence band edge	1.0×10^{20}/ 1.0×10^{20} cm^{-3}
E_R	trap energy level relative to conduction band	0.08 eV
N_R	density of trap sites	1.0×10^{19} cm^{-3}
S_n/S_p	electron/hole capture cross-section	3.8×10^{-18}/ 3.8×10^{-18} cm^{-2}
ν	thermal velocity	2.6×10^5 m/s

Now we will briefly discuss the physical picture of charge recombination processes in the presence of trap sites. Generally, recombination via trap states is through two serial processes: electron capture and hole capture. The capture rates and thus the carrier lifetime are determined by the electron population of the trap sites. We consider two situations: (1) The film is n-type and E_F lies below E_R. Here, E_F is located at position A as shown in Figure 6c. When increasing V_G from 0 to 50 V, E_F increases from E_i toward E_R and the electron occupancy of the trap sites increases. Since more electrons are available in the trap sites to capture holes, the minority carrier (hole) lifetime decreases. This agrees with observation (i). (2) The film switches from n-type to p-type. In this case, E_F is located at position B as shown in Figure 6c,d. The minority carrier (electron) lifetime in a p-type film is proportional to the hole occupancy of the trap sites. Because the trap sites are close to E_C, the hole occupancy is nearly 100%, much higher than the electron occupancy when the film is n-type. Thus, the minority carrier lifetime in the p-type film is much shorter than that in the n-type film, consistent with observation (ii). Therefore, the SRH model is consistent with both of the principal observations. In addition, the model suggests that most dark electrons are trapped in the n-type QD thin films. Otherwise, the minority carriers (holes) in the n-type film would quickly recombine with free electrons, which is inconsistent with the observed long lifetime. In this picture, the dark conductivity of an n-type QD thin film mainly involves electron tunneling between trap states. We note that midgap states have recently been suggested to participate in dark charge transport.[37] Further investigation is necessary to clarify the charge transport mechanisms. For example, spectroscopic methods can be used to measure the electron population in the core states, and more comprehensive modeling that considers multiple trap levels can be performed.

In summary, we have used SPCM to investigate the spatially resolved photocurrent of air-stable, ALD-infilled PbSe QD FETs. The strong gate dependence allows the investigation of charge transport and recombination as a function of carrier concentration and type. We have observed a photocurrent decay length up to 1.7 μm, which decreases to <0.5 μm as the carrier concentration is increased by V_G in n-type QD films. On the other hand, in p-type films, the photocurrent decay length is always short. By combining SPCM, KPM, and numerical modeling, we have shown that the thermoelectric and drift currents at the contacts cannot explain the long photocurrent decay length; rather, it results from the diffusion of a relatively small number of long-lived minority carriers. We emphasize that the diffusion length measured here applies to only a small fraction of the photogenerated carriers. Although most photogenerated carriers rapidly recombine, probably via midgap trap-assisted processes, a small fraction of photogenerated charges become trapped, likely at the surface of the QDs. These trapped charges have a much longer lifetime as confirmed by time-resolved photocurrent measurements. This long minority carrier decay length indicates that trap states for majority carriers can significantly slow the recombination of minority carriers and thereby extend the minority carrier diffusion length in QD thin films.

■ ASSOCIATED CONTENT

Supporting Information

Photocurrent time traces for device **D3**. This material is available free of charge via the Internet at http://pubs.acs.org.

■ AUTHOR INFORMATION

Corresponding Author

*E-mail: yu@physics.ucdavis.edu.

Author Contributions

T.O. and C.M. contributed equally to this work. J.T., Y.L., and M.L. synthesized PbSe QDs and fabricated ALD-infilled QD FETs. T.O., C.M., and D.Y. performed SPCM measurements and modeling. The manuscript was written with contributions from all authors.

Notes

The authors declare no competing financial interest.

■ ACKNOWLEDGMENTS

This work was supported by the U.S. National Science Foundation Grant NSF-1310678. J.T. acknowledges support from an NSF Graduate Research Fellowship. Y.L. and M.L. are supported by the Center for Advanced Solar Photophysics (CASP), an Energy Frontier Research Center funded by the U.S. Department of Energy (DOE), Office of Science, Office of Basic Energy Sciences (BES).

■ REFERENCES

(1) Johnston, K. W.; Pattantyus-Abraham, A. G.; Clifford, J. P.; Myrskog, S. H.; Hoogland, S.; Shukla, H.; Klem, E. J. D.; Levina, L.; Sargent, E. H. *Appl. Phys. Lett.* **2008**, *92* (12), 122111−3.
(2) Konstantatos, G.; Howard, I.; Fischer, A.; Hoogland, S.; Clifford, J.; Klem, E.; Levina, L.; Sargent, E. H. *Nature* **2006**, *442* (7099), 180−183.
(3) Luther, J. M.; Law, M.; Beard, M. C.; Song, Q.; Reese, M. O.; Ellingson, R. J.; Nozik, A. J. *Nano Lett.* **2008**, *8* (10), 3488−3492.
(4) Ellingson, R. J.; Beard, M. C.; Johnson, J. C.; Yu, P.; Micic, O. I.; Nozik, A. J.; Shabaev, A.; Efros, A. L. *Nano Lett.* **2005**, *5* (5), 865−871.
(5) Nozik, A. J. *Physica E* **2002**, *14*, 115−120.
(6) Nozik, A. J. *Chem. Phys. Lett.* **2008**, *457*, 3−11.
(7) Pandey, A.; Guyot-Sionnest, P. *Science* **2008**, *322* (5903), 929−932.
(8) Choi, J.-H.; Fafarman, A. T.; Oh, S. J.; Ko, D.-K.; Kim, D. K.; Diroll, B. T.; Muramoto, S.; Gillen, J. G.; Murray, C. B.; Kagan, C. R. *Nano Lett.* **2012**, *12* (5), 2631−2638.
(9) Dayeh, S. A.; Soci, C.; Yu, P. K. L.; Yu, E. T.; Wang, D. *Appl. Phys. Lett.* **2007**, *90* (16), 162112−3.
(10) Lee, J.-S.; Kovalenko, M. V.; Huang, J.; Chung, D. S.; Talapin, D. V. *Nat. Nanotechnol.* **2011**, *6* (6), 348−352.
(11) Liu, Y.; Gibbs, M.; Puthussery, J.; Gaik, S.; Ihly, R.; Hillhouse, H. W.; Law, M. *Nano Lett.* **2010**, *10* (5), 1960−1969.
(12) Luther, J. M.; Law, M.; Song, Q.; Perkins, C. L.; Beard, M. C.; Nozik, A. J. *ACS Nano* **2008**, *2* (2), 271−280.
(13) Talapin, D. V.; Murray, C. B. *Science* **2005**, *310* (5745), 86−89.
(14) Wehrenberg, B. L.; Yu, D.; Ma, J.; Guyot-Sionnest, P. *J. Phys. Chem. B* **2005**, *109* (43), 20192−20199.
(15) Yu, D.; Wang, C.; Wehrenberg, B. L.; Guyot-Sionnest, P. *Phys. Rev.* **2004**, *92* (21), 216802.
(16) Yu, D.; Wehrenberg, B. L.; Jha, P.; Ma, J.; Guyot-Sionnest, P. *J. Appl. Phys.* **2006**, *99* (10), 104315−7.
(17) Liu, Y.; Tolentino, J.; Gibbs, M.; Ihly, R.; Perkins, C. L.; Liu, Y.; Crawford, N.; Hemminger, J. C.; Law, M. *Nano Lett.* **2013**, *13* (4), 1578−1587.
(18) Ahn, Y.; Dunning, J.; Park, J. *Nano Lett.* **2005**, *5* (7), 1367−1370.
(19) Ahn, Y. H.; Tsen, A. W.; Kim, B.; Park, Y. W.; Park, J. *Nano Lett.* **2007**, *7* (11), 3320−3323.
(20) Graham, R.; Miller, C.; Oh, E.; Yu, D. *Nano Lett.* **2011**, *11* (2), 717−722.
(21) Graham, R.; Yu, D. *Nano Lett.* **2012**, *12* (8), 4360−4365.
(22) Gu, Y.; Romankiewicz, J. P.; David, J. K.; Lensch, J. L.; Lauhon, L. J. *Nano Lett.* **2006**, *6* (5), 948−952.
(23) Miller, C.; Triplett, M.; Lammatao, J.; Suh, J.; Fu, D.; Wu, J.; Yu, D. *Phys. Rev. B* **2012**, *85* (8), 085111.
(24) Strasfeld, D. B.; Dorn, A.; Wanger, D. D.; Bawendi, M. G. *Nano Lett.* **2012**, *12* (2), 569−575.
(25) Yang, Y.; Li, J.; Wu, H.; Oh, E.; Yu, D. *Nano Lett.* **2012**, *12* (11), 5890−5896.
(26) Fischbein, M. D.; Puster, M.; Drndic, M. *Nano Lett.* **2010**, *10* (6), 2155−2161.
(27) Hu, Z.; Fischbein, M. D.; Drndić, M. *Nano Lett.* **2005**, *5* (7), 1463−1468.
(28) Leatherdale, C. A.; Kagan, C. R.; Morgan, N. Y.; Empedocles, S. A.; Kastner, M. A.; Bawendi, M. G. *Phys. Rev. B* **2000**, *62* (4), 2669−2680.
(29) Moreels, I.; Lambert, K.; De Muynck, D.; Vanhaecke, F.; Poelman, D.; Martins, J. C.; Allan, G.; Hens, Z. *Chem. Mater.* **2007**, *19* (25), 6101−6106.
(30) Wang, R. Y.; Feser, J. P.; Lee, J.-S.; Talapin, D. V.; Segalman, R.; Majumdar, A. *Nano Lett.* **2008**, *8* (8), 2283−2288.
(31) Liang, W.; Rabin, O.; Hochbaum, A.; Fardy, M.; Zhang, M.; Yang, P. *Nano Res.* **2009**, *2* (5), 394−399.
(32) Bube, R. H. *Photoconductivity of Solids*; John Wiley & Sons, Inc.: New York, 1960; pp 312−314.
(33) Bittmann, C. A.; Bemski, G. *J. Appl. Phys.* **1957**, *28* (12), 1423−1426.
(34) Burton, J. A.; Hull, G. W.; Morin, F. J.; Severiens, J. C. *J. Phys. Chem.* **1953**, *57* (8), 853−859.
(35) Erslev, P. T.; Chen, H.-Y.; Gao, J.; Beard, M. C.; Frank, A. J.; van de Lagemaat, J.; Johnson, J. C.; Luther, J. M. *Phys. Rev. B* **2012**, *86* (15), 155313.
(36) Guyot-Sionnest, P. *J. Phys. Chem. Lett.* **2012**, *3* (9), 1169−1175.
(37) Nagpal, P.; Klimov, V. I. *Nat. Commun.* **2011**, *2*, 486.